

0418

# Research and Application in Finite Volume Time Domain Electromagnetics

## Final Technical Report

October 14, 1994 through July 14, 1997

Contract No. F49620-95-C-0006

Prepared for:

Air Force Office of Scientific Research/NM  
Directorate of Mathematics and Geosciences  
110 Duncan Avenue - Suite B115  
Bolling AFB, DC 20332-0001  
Attn: Dr. Arje Nachman

Prepared by:

W.F. Hall, Principal Investigator, A.H. Mohammadian,  
C.M. Rowell and V. Shankar

Rockwell Science Center, LLC  
1049 Camino Dos Rios  
Thousand Oaks, CA 91360  
April 1998

DRAFT COPY UNCLASSIFIED 4



Science Center

19980505 006

Copy # 1

REPORT DOCUMENTATION PAGE			Form Approved OMB No. 0704-0188	
Public reporting burden for this collection of information is estimated to average 1 hour per response, including the time for reviewing instructions, searching existing data sources, gathering and maintaining the data needed, and completing and reviewing the collection of information. Send comments regarding this burden estimate of any other aspect of this collection of information, including suggestions for reducing this burden, to Washington Headquarters Services, Directorate for Information Operations and Reports, 1215 Jefferson Davis Highway, Suite 1204, Arlington, VA. 22202-4302, and to the Office of Management and Budget, Paperwork Reduction Project (0704-0188), Washington, DC 20503				
1. AGENCY USE ONLY (Leave Blank)		2. REPORT DATE March 1998	3. REPORT TYPE AND DATES COVERED Final Technical Report 10/14/94-07/14/97	
4. TITLE AND SUBTITLE Research and Application in Finite Volume Time Domain Electromagnetics			5. FUNDING NUMBERS C F49620-95-C-0006	
4. AUTHOR(S) Hall, W.F.				
7. PERFORMING ORGANIZATION NAME(S) AND ADDRESS(ES) ROCKWELL SCIENCE CENTER, LLC 1045 CAMINO DOS RIOS THOUSAND OAKS, CA 91360			7. PERFORMING ORGANIZATION REPORT NUMBER SC 71105.FTR	
9. SPONSORING / MONITORING AGENCY NAME(S) AND ADDRESS(ES) AFOSR/NM Directorate of Mathematics and Geosciences 110 Duncan Ave., Ste. B115 Bolling AFB, DC 20332-0001 Attn: Dr. Arje Nachman			9. SPONSORING / MONITORING AGENCY REPORT NUMBER	
11. SUPPLEMENTARY NOTES				
12a. DISTRIBUTING/AVAILABILITY STATEMENT  Approved for public release, distribution unlimited			12b. DISTRIBUTION CODE	
13. ABSTRACT (Maximum 200 Words) <p>The development of an accurate time-domain solution technique for Maxwell's equations suitable for simulation of large radar ranges is described. This technique is a finite-volume method that maintains high-order accuracy on unstructured meshes that can be generated automatically. It is being applied to the RAMS site at Holloman Air Force Base, New Mexico, to help determine effects of the target support and the topography of the site on the measured radar return at low frequencies, up to 600MHz. Especially for low-observable targets, these effects may dominate the return.</p> <p>The report includes examples of the first application of the solution technique to large, unstructured 3D grids, as well as a determination of the fields incident on the target and its support as the solution of a large 2D scattering problem. This 2D simulation extends over a distance of a few hundred feet in the direction of propagation and includes topographic details of the pit in which the target support is mounted.</p> <p>The simulations have been performed on massively parallel computer architectures, such as the IBM SP2, where the solution technique exhibits essentially ideal scaling with the number of processors used.</p>				
14. SUBJECT TERMS Electromagnetics, radar cross-section (RCS), radar ranges, computational methods, partial differential equations, high-performance computing, finite-volume, time domain, unstructured grid			15. NUMBER OF PAGES 31	
			16. PRICE CODE	
17. SECURITY CLASSIFICATION OF REPORT UNCLASSIFIED	18. SECURITY CLASSIFICATION OF THIS PAGE UNCLASSIFIED	19. SECURITY CLASSIFICATION OF ABSTRACT UNCLASSIFIED	20. LIMITATION OF ABSTRACT SAR	

**Table of Contents**

	<b>Page</b>
<b>1 Summary .....</b>	<b>1</b>
<b>2 Introduction .....</b>	<b>1</b>
<b>3 Methods, Assumptions, and Procedures .....</b>	<b>3</b>
3.1 The RAMS Range: Stages of Simulation .....	3
3.2 Numerical Method .....	5
3.2.1 <i>General Considerations</i> .....	5
3.2.2 <i>Finite-Volume Integration</i> .....	7
3.2.3 <i>Time Integration Alternatives</i> .....	9
3.2.4 <i>Taylor Series Reconstruction</i> .....	14
3.2.5 <i>Evaluating the Face Integrals</i> .....	16
<b>4 Results and Discussion .....</b>	<b>18</b>
4.1 Incident Field Computation .....	18
4.2. 3 D Scattering Simulation: ORCA Target on the RAMS Pylon .....	21
4.3 Grid Sensitivity Test: The Business Card .....	24
<b>5 Conclusions .....</b>	<b>26</b>
<b>6 References .....</b>	<b>27</b>

## List of Figures

1	Profile of the RAMS shadow-plane range near the target. The upper flat section is inclined about 1.4 degrees from the horizontal.....	3
2	2D idealization of the RAMS site showing a plane wave scattering off the upper half-plane and the reflection of this solution in the ground plane. The insert shows a top view of the ridge profile and its orientation with respect to the line of sight between the radar and the target.....	4
3	Unstructured triangular grid in the vicinity of the diffraction ridge.....	20
4	Snapshot of the numerically generated diffracted electric field, which modifies the two half-plane solutions to produce the wave incident on the target and its support.....	21
5	Snapshot of the total electric field for the same conditions as in Fig. 4.....	21
6	ORCA and pylon 3D gridding: a) ORCA/pylon geometry; b) Surface grid on ORCA and pylon; c) The triangular grid on the symmetry plane behind the pylon; d) Symmetry plane grid near the ridge .....	23
7	Scattered E field (component parallel to ridge line) within the shadow pit at 131 MHz for H-polarized incident wave .....	24
8	Total E field (component parallel to ridge line) within the shadow pit at 131 MHz for H-polarized incident wave .....	24
9	Grid Insensitivity of UPRCS: Comparison of business card RCS results for an unstructured and a structured grid with range measurements.....	25

## 1. Summary

This final technical report summarizes the results of research performed under Air Force Contract No. F49620-95-C-0006 to develop the capability for accurate simulation of the RCS measurement process on high-quality radar ranges, and specifically for the RAMS shadow-plane range at Holloman Air Force Base, New Mexico. The general goal of such simulations is to determine the magnitude of effects due to the range and the target support on the measurements, and to evaluate modifications to the range design that can alleviate such effects. An approach has been developed that allows detailed simulations to be performed on existing massively parallel computers for the RAMS range at radar frequencies up to 600 MHz.

One paper was published, one has been submitted for publication, and four technical conference presentations were made during this effort. Extensive 2D simulations of a shadow plane range were performed using a range profile derived from a topographic map of the RAMS site provided by the 46<sup>th</sup> Test Group at Holloman Air Force Base. The first 3D simulations of a low-observable target on a pylon in the RAMS shadow pit were carried out using a new unstructured-grid time-domain integration scheme developed as part of this research.

It is anticipated that significant applications of this work will be made in the near future to support redesign and upgrades for RAMS. Applications to other radar ranges should also be pursued.

## 2. Introduction

The large size of far-field radar ranges poses a serious problem for any numerical method that seeks an accurate solution to Maxwell's equations for the fields scattered back to the radar from the vicinity of the target and its supporting structure. Even compact ranges are typically an order of magnitude larger in every dimension than the targets they measure, so that

the number of unknowns required for direct numerical solution is two to three orders of magnitude larger than that for the target alone. Since numerical techniques have only recently advanced to the point where the radar cross-section (RCS) of an isolated low-observable (LO) aircraft can be accurately computed at wavelengths shorter than one meter, it is clear that a considerable improvement in solution methods will be required.

The approach taken in the current effort treats separately the processes of radiation from the source radar, propagation over the range, scattering from the neighborhood of the target, and propagation back to the radar. A unique, general 3D solver for Maxwell's equations in the time domain has been developed to determine the scattered fields. This solver is almost ideally suited for massively parallel computing platforms, exhibiting linear speedup over two orders of magnitude in the number of processors used.

The specific application driving this research has been the continuing effort to improve the capabilities of the RAMS radar range at Holloman Air Force Base in New Mexico. Especially for low-observable (LO) targets at frequencies below 600 MHz, there is concern that interactions among the target, its support, and the surrounding range modify the target return to a significant extent. To address this concern, the 46<sup>th</sup> Test Group at Holloman is pursuing a number of experimental approaches, including the use of a specially-designed LO target.

Numerical simulation of the range offers a way to compare the benefits of these different approaches, and to explore effects within a wide range of experimentally accessible conditions. Quantitative studies can reveal the best directions for redesign of the target support or the presence of unwanted effects due to modifications of the range profile.

The particular approach developed in the research reported here employs explicit time integration in a finite-volume framework for an unstructured grid [1]. This method, which draws heavily on the foundations of similar techniques current in computational fluid

dynamics, is an outgrowth of ongoing work at the Rockwell Science Center on time-domain computation of radar scattering from isolated targets [2].

### 3. Methods, Assumptions, and Procedures

#### 3.1 The RAMS Range: Stages of Simulation

The RAMS range uses a depression in the ground to hide the base of the target support from the illuminating radar. As shown in Fig. 1, a steep ridge (known as the diffraction ridge) connects the lower ground plane with the upper plane on which the illuminating radar sits. This ridge is horizontal, but inclined about 70 degrees from the line of sight between the radar and the target. Thus, the simulation of ridge effects is inherently three-dimensional.

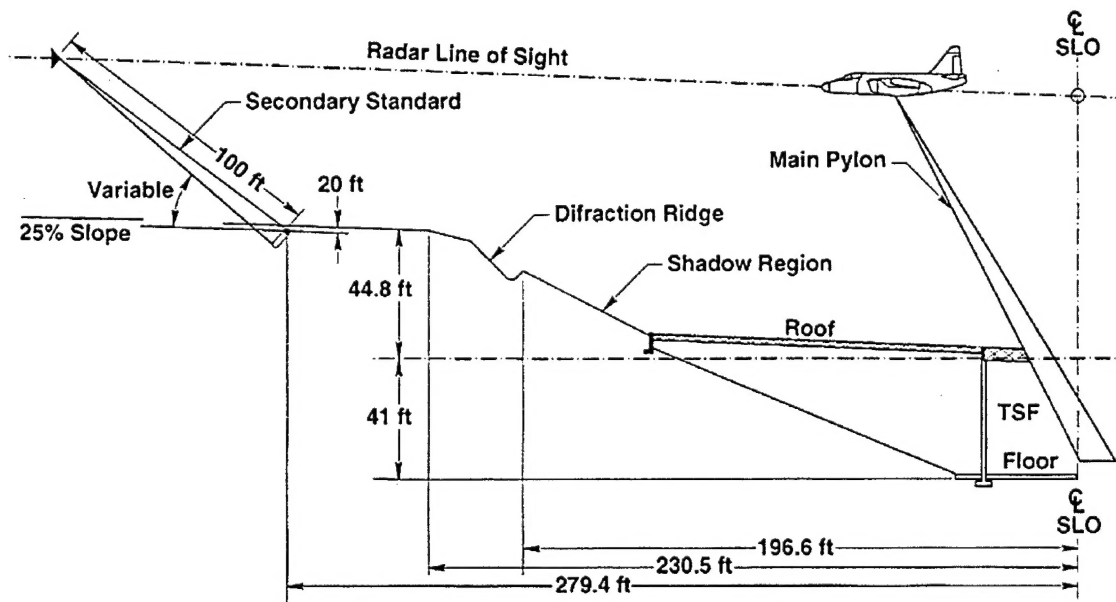


Fig. 1. Profile of the RAMS shadow-plane range near the target. The upper flat section is inclined about 1.4 degrees from the horizontal.

The simulation of the ridge, the depression, the target support, and the target has been divided into two stages. In the first stage, the modifications of the incident plane wave by the ridge profile are determined, while in the second stage, this modified incident wave is scattered

off the target and its support. The resulting surface currents on the range, the target, and the support are then used to calculate the radar return.

The first stage simulation uses a dense, relatively uniform 2D grid between the ridge and the location of the target support in order to minimize any numerical damping of the waves that diffract off the ridge and illuminate the target and its support. The target and support are not included in the simulation, but the field values at their location are stored for use in the second stage.

The incident field input for the first stage simulation is constructed from the Sommerfeld half-plane solution for the upper ground plane, and for its reflection in the lower ground plane, as sketched in Fig. 2. Subtracting these two fields from the total field restricts the source currents for the remainder to the near vicinity of the ridge, where they can be accurately resolved by the grid. At the boundary of the computational domain, this remainder field is an outgoing wave, so reflections from this boundary are minimized by the methods developed for pure scattering problems: stretching of the grid near this boundary and zeroing of the combination of field components that represents waves incoming along the normal to the boundary surface [2].

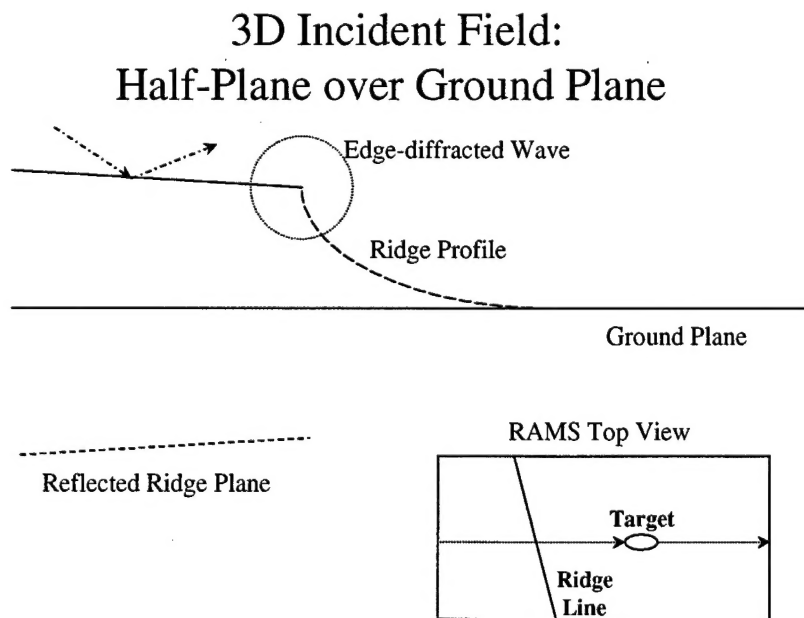


Fig. 2. 2D idealization of the RAMS site showing a plane wave scattering off the upper half-plane and the reflection of this solution in the ground plane. The insert shows a top view of the ridge profile and its orientation with respect to the line of sight between the radar and the target.



For the second stage of the simulation, a 3D grid clustered about the target and its support is constructed. Although a portion of the ridge is included in the grid, it is assumed that one can neglect the secondary illumination of the target by waves scattered from the target to the ridge and back. The computed values of this minor contribution will be weakened by the stretching of the grid away from the target. The current sources for the fields scattered by the target and its support will be strong only on the target and support and around the base of the support, where the grid is clustered.

This two-stage strategy greatly reduces the number of grid cells needed to do accurate range simulations. The 2D grid, which at 600 MHz extends for perhaps 150 wavelengths along the ground plane and 100 wavelengths vertically, should require at most a few million grid cells to obtain good accuracy in the fields on the target. The 3D grid, due to clustering around the target, is of the same order. These simulations can be run efficiently on 128 nodes of the IBM SP2 or any comparable parallel architecture.

## **3.2 Numerical Method**

### ***3.2.1 General Considerations***

A principal objective of this research effort is to extend the capability for numerical solution of Maxwell's equations through the development of more efficient integration algorithms, and specifically algorithms that are robust and accurate on automatically-generated unstructured grids. Gridding is a major issue: the application of numerical methods to scattering from complex targets has been seriously restricted by the magnitude of the effort that is required to develop a discretization of the geometry compatible with the numerical method that adequately resolves the significant features of the true solution without creating a numerical problem that exceeds the available memory or CPU time.

A Cartesian discretization is trivial to create, but it replaces the actual target boundary with a stair-cased surface that impacts solution accuracy in ways that are difficult to analyze. Also, the number of Cartesian cells in the grid scales with the highest resolution required on (or

inside) the target, so that electrically large problems incorporating fine detail are beyond the reach of today's massively parallel computers. Despite these limitations, it is the basis for the most widely exploited time-domain solution method in electromagnetics, the Yee algorithm [3]. This algorithm uses two interpenetrating grids in space, one each for the electric and magnetic fields, and staggers the field unknowns in time, advancing the solution by the "leapfrog" approach.

Generalizations of the Yee algorithm to non-Cartesian grids have been implemented for various types of problems [4-6]. However, the major advantage of simplicity in defining the grid is lost, while a theoretical basis for analyzing the stability and accuracy of these schemes has yet to be developed. Numerical experiment is required to verify that the solution is not too sensitive to details of the grid, so that gridding once again presents a significant bottleneck in the use of these methods.

A quite different approach to the time integration of partial differential equations has been pursued in computational fluid dynamics (CFD). Flow around an obstacle is discretized on a single volume grid, fitted to the body surface and expanding in cell size toward the outer boundary of the computational domain, where an appropriate free-stream condition is imposed. (An overlapping grid may also be defined to simplify the propagation of information from one densely-gridded region to another.) Originally developed for grids consisting of collections of distorted Cartesian blocks, these methods have in recent years been extended to unstructured grids [7-9].

The present work is based largely on the ideas behind the CFD approach to time integration on arbitrary grids. The primary difference in emphasis is that time accuracy is a major requirement in integrating Maxwell's equations, while often only steady-state solution properties are sought in CFD. Propagating waves accurately between different parts of a target is a serious concern in computing the radar cross-section (RCS) of complex targets. It shares

many features with the problem of aero-acoustics in CFD, as has been recognized by Roe and his collaborators [10].

Methods for the automatic generation of unstructured grids have primarily been developed to support the finite-element solution technique, which is widely popular in structural mechanics [11]. This method now has a firm mathematical basis, and it is being applied to both fluid dynamics and electromagnetics in a variety of contexts. While recent studies of time-accurate integration for electromagnetics are promising [11,12], the sensitivity of the finite-element technique to irregularities in the grid remains to be established for wave propagation. It is an unfortunate feature of the automatic generation methods that many grid cells are created having extreme aspect ratios among the edge lengths of the cell, and such irregular cells are often found near the target surfaces.

The family of time integration methods developed in the present work can be considered as finite-volume schemes, in the sense that the basic unknowns represent averages of the continuum solution over each cell in the grid. To advance these unknowns to the next time level, approximations for the solution at the cell boundary are formed from the neighbor cell averages, and these approximations are integrated in a manner consistent with the underlying partial differential equation to give an estimate for the time increment in each unknown. Predictor-corrector or Runge-Kutta schemes are then used to combine various estimates in such a way that the desired degree of accuracy in both time and space is maintained in the final update.

A preliminary study has been made of the accuracy and stability properties of these methods for unstructured grids [13]. Results for one spatial dimension indicate that good wave propagation characteristics are achievable at moderate average spatial resolution on periodic grids that stretch and compress by a factor of four or more. Numerical experiments in two and three dimensions confirm these observations, and recent results included in this report show that grid sensitivity has been greatly reduced.

### 3.2.2 Finite-Volume Integration

Maxwell's curl equations for the electromagnetic fields in a material medium can be written in SI notation as either local first-order partial differential equations or as integrals over an arbitrary volume  $V$  bounded by a regular surface  $\partial V$ :

#### Differential Form

$$\partial \mathbf{B} / \partial t = -\nabla \times \mathbf{E}, \quad (1a)$$

$$\partial \mathbf{D} / \partial t = \nabla \times \mathbf{H} - \mathbf{J} \quad (1b)$$

#### Volume Integral Form

$$d[\int_V \mathbf{B} \, dV] / dt = - \int_{\partial V} \mathbf{n} \times \mathbf{E} \, dS, \quad (1c)$$

$$d[\int_V \mathbf{D} \, dV] / dt = \int_{\partial V} \mathbf{n} \times \mathbf{H} \, dS - \int_V \mathbf{J} \, dV, \quad (1d)$$

where  $\mathbf{B}$  is the magnetic induction,  $\mathbf{D}$  is the electric displacement,  $\mathbf{E}$  is the electric field,  $\mathbf{H}$  is the magnetic field,  $\mathbf{J}$  is the electric current, and  $\mathbf{n}$  is the outward-pointing unit normal to  $\partial V$ . These equations are supplemented by the conditions  $\nabla \cdot \mathbf{B} = 0$  and  $\nabla \cdot \mathbf{D} = \rho$ , where the electric charge density  $\rho$  obeys the basic conservation law  $\partial \rho / \partial t = -\nabla \cdot \mathbf{J}$ . These two relations can be regarded as initial conditions, since the curl equations guarantee that the time increments in  $\mathbf{B}$  and  $\mathbf{D}$  will also satisfy the conditions.

For purposes of exposition, this section of the report considers propagation in free space, where  $\mathbf{J}$  vanishes,  $\mathbf{D} = \epsilon_0 \mathbf{E}$ , and  $\mathbf{B} = \mu_0 \mathbf{H}$  (where  $\epsilon_0$  and  $\mu_0$  are the permittivity and permeability of vacuum, respectively). The principles described below apply equally well to material media, but the relations among the field variables are generally more complicated.

It is convenient to write for  $\mathbf{B}$  and  $\mathbf{D}$  a single "vector"  $\mathbf{Q}$  of six field components, and to define a tensor flux  $\mathbf{F}(\mathbf{E}, \mathbf{H})$  in terms of which Maxwell's equations can be written in standard conservation form:

#### Conservation Form

$$\mathbf{Q} = (\mathbf{B}, \mathbf{D}) \quad (2a)$$

$$\mathbf{F}_x = (\mathbf{i} \times \mathbf{E}, -\mathbf{i} \times \mathbf{H}), \quad \mathbf{F}_y = (\mathbf{j} \times \mathbf{E}, -\mathbf{j} \times \mathbf{H}), \quad \mathbf{F}_z = (\mathbf{k} \times \mathbf{E}, -\mathbf{k} \times \mathbf{H}) \quad (2b)$$

$$\partial \mathbf{Q} / \partial t + \nabla \cdot \mathbf{F}(\mathbf{Q}) = 0 \quad (2c)$$

In this way, the set of six equations is cast into the same mathematical structure as conservation of charge.

If one integrates  $\partial Q/\partial t + \nabla \cdot \mathbf{F}(\mathbf{Q}) = 0$  over each grid cell  $\alpha$ , the result is:

$$dQ_\alpha/dt = -\int_{\partial\alpha} \mathbf{n} \cdot \mathbf{F}(\mathbf{Q}(\mathbf{r},t)) dS / V_\alpha, \quad (3)$$

where  $Q_\alpha(t) \equiv \int_\alpha Q(\mathbf{r},t) dV/V_\alpha$ ,  $\partial\alpha$  is the boundary of cell  $\alpha$ ,  $V_\alpha$  is its volume, and  $\mathbf{n}$  is the outward-pointing unit normal to  $\partial\alpha$  at  $\mathbf{r}$ . In the present approach, this surface integral is implemented as a sum over all faces of the cell.

Finite-volume schemes differ on how they estimate  $Q$  on each face, and on how  $dQ/dt$  is used to update  $Q$ . Integration methods are limited by the accuracy with which the values for  $Q$  at a cell face are reconstructed from the volume averages  $Q_\alpha$ . Typical reconstruction schemes are second-order accurate on uniform grids. They incur lower order errors on grids where cell shapes are irregular.

### 3.2.3 Time Integration Alternatives

#### 3.2.3.1 Taylor Series in Time

In developing the second-order finite difference scheme that bears their names, Lax and Wendroff started from a Taylor series expansion of the solution  $u(x, t + \Delta t)$  in the time increment  $\Delta t$  and replaced the repeated time derivatives of  $u$  in this expansion with space derivatives of the flux  $f(u)$ , where the basic partial differential equation had the form:

$$\partial u/\partial t + \partial f(u)/\partial x = 0. \quad (4)$$

The space derivatives were then approximated by central differencing on a uniform grid. The values  $u(x_j, t_n)$  could be regarded either as approximations to the point values of  $u$  or as averages over each grid cell.

Extension of this approach to multidimensional unstructured grids and multicomponent unknowns  $Q$  is most naturally carried out in terms of cell averages. A Taylor series for  $Q_\alpha(t + \Delta t)$  can be written in terms of Eq. (3) and its higher time derivatives.

Evaluating a typical term in this series involves determining values for the function  $Q$  and its spatial derivatives up to some order at the boundary of the cell. The simplest schemes of this type advance only the cell averages to the next time level and approximate, or "reconstruct", the variation of  $Q$  within a cell from these averages.

The boundary values of the reconstructed function at the interface between two cells will in general differ, depending on from which side the interface is approached. Godunov suggested regarding this difference as a discontinuity in the actual solution, and proposed calculating the cell averages at the next time level by appropriately propagating this discontinuous field. This step involves solving a classical Riemann problem at each interface.

When  $F(Q)$  depends linearly on  $Q$ , as it does for Maxwell's equations in the limit of weak fields, the Riemann problem can be solved exactly in terms of the eigenfunctions and eigenvalues of the Jacobian matrix  $\partial F/\partial Q$ . Characteristic combinations of the elements of  $Q$  can be identified that propagate as simple waves  $w(\mathbf{n} \cdot \mathbf{r} \pm ct)$  across the interface. Expressing the discontinuity in  $Q$  in terms of these waves allows the behavior of  $Q$  at the interface for infinitesimally later times  $t + \varepsilon$  to be well approximated. Because the data determining this behavior are drawn only from the waves that propagate toward the interface from either side, this process is called "upwinding."

#### *3.2.3.2 Upwind Taylor Integration*

It is the upwind values for  $Q$  and its derivatives that enter into the surface integrals of Eq. (3) and its derivatives in the upwind Taylor scheme. To complete the description of the scheme, one needs to specify how  $Q$  is to be reconstructed in each cell from its averages. The

details of this procedure directly influence both the accuracy and stability of the overall algorithm, as well as its computational efficiency.

In the upwind Lax-Wendroff scheme [1], a linear variation of the solution in each cell is determined from upwind values for  $Q$  at the cell faces, calculated from the average values in the two cells neighboring each interface. This procedure doubles the size of the allowable time step, compared to the original Lax-Wendroff scheme, but it limits the accuracy of the reconstruction and adds considerable dissipation in cells large compared to the optimum size.

An alternative reconstruction procedure commonly employed in computational fluid dynamics starts from the assumption that the solution is smooth over a region encompassing many near neighbors of each cell, with continuous derivatives up to some order. The averages over neighboring cells are then expressible in terms of these derivatives, and a collection of these expressions is solved for the derivatives [7]. Real discontinuities in the solution, such as shock waves, complicate the choice of neighbors and may degrade the accuracy locally.

In electromagnetics, field discontinuities occur primarily at domain boundaries and material interfaces, the locations of which are known in advance. Appropriate boundary and interface conditions can be derived from Maxwell's equations, and these conditions can then be used to carry information into each cell neighboring such a boundary, provided the boundary is smooth. Near geometrical singularities, such as cracks and edges, the representation inside the cell may include singular functions. In regions away from physical boundaries it is feasible to assume smooth behavior of the fields, and this is the approach that has been followed in the current effort

#### *3.2.3.3 Runge-Kutta Integration Schemes for Maxwell's Equations*

The dissipation that is an inescapable part of upwinding can effectively be avoided by using central estimates for spatial derivatives. While Yee's scheme is the method of this type

most well-known to the electromagnetics community, Runge-Kutta central schemes have been widely exploited in computational fluid dynamics [9].

The essential difference between Lax-Wendroff schemes and those of Runge-Kutta type can be understood with reference to equation (3), which expresses the time derivative of the volume average  $Q_\alpha$  in terms of a surface integral of the flux. Rather than directly expanding  $Q_\alpha$  in a Taylor series in time, one regards (3) as a first-order system of ordinary differential equations for the set of unknown  $Q_\alpha$ 's. The estimate for  $Q(r, t)$  at the cell interface is expressed as a linear combination of the surrounding  $Q_\alpha$ 's, closing the system of equations, which can now be written

$$\frac{d}{dt} \underline{Q} = H(\underline{Q}), \quad (5)$$

where  $H$  is a sum over the flux from each face of the cell, and  $\underline{Q}$  is the set of unknown volume averages  $\{Q_\alpha\}$ . The lowest-order central estimate for  $Q$  at a cell face  $\alpha\beta$  is just  $(Q_\alpha + Q_\beta)/2$ . Note that, in contrast to the upwind Lax-Wendroff scheme, it uses no information about the characteristics of the flux.

The Runge-Kutta schemes for integrating a first-order system of the type (5) are explicit, single-step methods that involve constructing a number of intermediate estimates  $\underline{Q}^{(v)}$  at time levels between  $n$  and  $n+1$ . Each intermediate stage has the form

$$\underline{Q}^{(v)} = \underline{Q}^n + \mu_v \Delta t H(\lambda_{v1} \underline{Q}^{(v-1)} + \lambda_{v2} \underline{Q}^{(v-2)} + \dots), \quad (6)$$

with  $\underline{Q}^{(0)} = \underline{Q}^n$ , while the final update is written as

$$\underline{Q}^{n+1} = \underline{Q}^n + \Delta t [\alpha_0 H_0 + \alpha_1 H_1 + \dots + \alpha_{\kappa-1} H_{\kappa-1}], \quad (7)$$

where  $H_v = H(\lambda_{v1} \underline{Q}^{(v-1)} + \lambda_{v2} \underline{Q}^{(v-2)} + \dots)$  and  $\kappa$  is the number of stages in the scheme. Time accuracy up to the order of the number of stages is obtained with appropriate conditions on the coefficients  $\mu$ ,  $\lambda$ , and  $\alpha$ .



The advantage of Runge-Kutta schemes of third order and higher for wave propagation is that they need not damp oscillatory solutions: their region of stability includes purely real frequencies. When  $H$  is a linear function of  $Q$ , as it is for Maxwell's equations, each eigenvector  $E_\lambda$  of  $H$  will satisfy (5) with a time dependence  $e^{-i\omega t}$ :

$$-i\omega E_\lambda = H(E_\lambda) = \lambda E_\lambda , \quad (8)$$

where the eigenvalues  $\lambda$  are determined by the spatial discretization and the boundary conditions. For a central discretization on a uniform grid with periodic boundary conditions, all the eigenvalues are imaginary, and the eigenfunctions are in fact simple sinusoidal waves. Also, the set of eigenvectors of  $H$  spans the complete space of solutions for  $Q$ , so that any initial condition on  $Q$  can be represented by them.

For a general unstructured grid, the eigenvectors of  $H$  are not sinusoids, but a "central" discretization can still produce an imaginary eigenspectrum. In such a case, the Runge-Kutta methods will preserve the amplitude of any initial wave indefinitely. Its phase, however, will not track that of the exact solution, except at wavelengths long compared to the size of the grid cells, nor will the form of the wave remain sinusoidal, as the various eigenvectors composing the initial wave will have different characteristic frequencies. High-order central discretizations will, of course, preserve the phase over longer distances of propagation.

When high spatial frequencies are present in the initial conditions, for example in scattered-field computations with vanishing initial fields except at the target boundary, the lack of dissipation for high-frequency eigensolutions poses a problem. Although the behavior of these solutions bears very little resemblance to exact solutions of Maxwell's equations at these frequencies, they will continue to add unwanted structure to the solution indefinitely. To remove this structure, filtering procedures of various forms have been applied, including the addition of damping terms in (5) proportional to some high spatial derivative of the solution. Filters with very little damping at long wavelengths can be implemented in this way.

In the current effort a simple filter implemented by Jameson [9] that models the fourth spatial derivatives of the solution has been implemented. On a regular grid, this filter reduces to an estimate for  $\nabla^4 Q$ , constructed in a two-step process from the neighbor volume averages. On general grids, lower order derivatives contribute significantly to the filter. As part of developing the new code UPRCS, the effect of this damping term on stability and accuracy has been investigated in a series of numerical experiments, and a suitable range for its magnitude has been determined.

The form of the fourth-order damping term, denoted  $D^4 Q$ , can be represented as a sum over all faces of the parent cell  $\alpha$ :

$$D^4 Q_\alpha = K \sum_{\text{faces}} [D^2 Q_\beta - D^2 Q_\alpha], \quad (9)$$

where  $K$  is a constant determined by numerical experiment, typically  $1/256$ , and  $D^2 Q$  is given by

$$D^2 Q_\alpha = \sum_{\text{faces}} [Q_\beta - Q_\alpha] \quad (10)$$

This damping term is added to each of the four stages of the Runge-Kutta time integration procedure.

### 3.2.4 Taylor Series Reconstruction

Inside Cell  $\alpha$ , the fields are assumed to be analytic functions of  $\mathbf{r}$ :

$$Q(\mathbf{r}, t) = Q(\mathbf{r}_\alpha, t) + \sum_{lmn} [\partial_x^l \partial_y^m \partial_z^n Q(\mathbf{r}_\alpha, t)] (x-x_\alpha)^l (y-y_\alpha)^m (z-z_\alpha)^n / l! m! n! \quad (11)$$

where  $\mathbf{r}_\alpha$  is the centroid of cell  $\alpha$  and, e.g.,  $\partial_x$  stands for  $\partial/\partial x$ . At the cell surface each normal and tangential component of these derivatives satisfies a continuity condition involving the values of  $\epsilon$  and  $\mu$  on either side of the interface. Using these conditions, the variation of  $Q$  inside each neighbor cell  $\beta$  can be written in terms of its expansion inside cell  $\alpha$ . For simplicity, this section considers free space cells, for which there are no discontinuities in the derivatives.

Matching the volume integral of the Taylor expansion over a neighbor cell  $\beta$  to the known volume average  $Q_\beta$  gives a condition on the derivatives of  $Q$  in terms of the geometric moments  $M_\beta^{lmn}$  of the cell about  $\mathbf{r}_\alpha$ :

$$Q_\beta(t) = Q(\mathbf{r}_\alpha, t) + \sum_{lmn} [\partial_x^l \partial_y^m \partial_z^n Q(\mathbf{r}_\alpha, t)] M_\beta^{lmn}(\mathbf{r}_\alpha) / l!m!n! , \quad (12)$$

where

$$M_\beta^{lmn}(\mathbf{r}_\alpha) = \int_\beta (x-x_\alpha)^l (y-y_\alpha)^m (z-z_\alpha)^n dV/V_\beta \quad (13)$$

For any set of neighbor cells, the differences  $Q_\beta - Q_\alpha$  thus can be expressed in terms of these moments and the derivatives of  $Q$  at  $\mathbf{r}_\alpha$ :

$$Q_\beta(t) - Q_\alpha(t) = \sum_{lmn} [\partial_x^l \partial_y^m \partial_z^n Q(\mathbf{r}_\alpha, t)] [M_\beta^{lmn}(\mathbf{r}_\alpha) - M_\alpha^{lmn}(\mathbf{r}_\alpha)] / l!m!n! . \quad (14)$$

Each difference has the form of a scalar product  $DQ_\alpha \cdot DM_\beta$  between the unknown derivative "vector"  $[\partial_x^l \partial_y^m \partial_z^n Q_\alpha]$  and a moment "vector"  $[M_\beta^{lmn} - M_\alpha^{lmn}]$  determined by the local cell geometry. These are vectors in an infinite-dimensional space  $\Omega$  where the scalar product is defined as:

$$A \cdot B = \sum_{lmn} A^{lmn} B^{lmn} / l!m!n! \quad (15)$$

The whole set of differences can be regarded as determining the projection of  $DQ_\alpha$  onto the subspace of  $\Omega$  spanned by the collection of neighbor moment vectors  $\{DM_\beta\}$ . The components of  $DQ_\alpha$  that are orthogonal to all the  $DM_\beta$ 's are undetermined.

One can summarize all this by writing

$$\partial_x^l \partial_y^m \partial_z^n Q_\alpha = \sum_{\beta} A_{\alpha}^{\beta} [M_{\beta}^{lmn}(\mathbf{r}_{\alpha}) - M_{\alpha}^{lmn}(\mathbf{r}_{\alpha})] + R_{\alpha}, \quad (16)$$

where  $R_{\alpha} \cdot DM_{\beta} = 0$  for each neighbor  $\beta$ , and the coefficients  $A_{\alpha}^{\beta}$  are linear combinations of the differences  $Q_{\beta} - Q_{\alpha}$ , found from the known scalar products as:

$$A_{\alpha}^{\beta} = [DM_{\beta} \cdot DM_{\gamma}]^{-1} [Q_{\gamma} - Q_{\alpha}] = \sum_{\gamma} \alpha_{\alpha}^{\beta\gamma} [Q_{\gamma} - Q_{\alpha}]. \quad (17)$$

In what follows, we will take  $R_{\alpha} = 0$ . More generally, one can choose  $R_{\alpha}$  to satisfy the divergence conditions on B and D, while minimizing its total "length,"  $R_{\alpha} \cdot R_{\alpha}$ .

### 3.2.5 Evaluating the Face Integrals

At the interface  $\alpha\beta$  between cell  $\alpha$  and cell  $\beta$ , the flux  $F(Q(\mathbf{r},t))$  will use values for  $Q$  derived from both sides, i.e., from the two derivative vectors  $DQ_{\alpha}$  and  $DQ_{\beta}$ . The specific time integration scheme will determine a linear combination  $Q^*$  of the two Taylor series to replace  $Q(\mathbf{r},t)$  in the argument of  $F$ : for an upwind scheme,  $Q^*$  will be the Riemann combination, while

for centered Runge-Kutta schemes,  $Q^*$  will normally be the arithmetic average. To allow for both possibilities, we shall write  $Q^* = c_\alpha Q^\alpha + c_\beta Q^\beta$  with constants  $c$  determined by the scheme.

Since the Maxwell flux is linear in  $Q$ , integrating  $F$  over the face  $\alpha\beta$  consists of integrating each piece of  $Q^*$  separately:

$$\int_{\alpha\beta} \mathbf{n} \cdot \mathbf{F}(Q^*) dS = \mathbf{n}_{\alpha\beta} \cdot \frac{\partial F}{\partial Q} \int_{\alpha\beta} \{c_\alpha [Q(\mathbf{r}_\alpha, t) + DQ_\alpha \cdot \mathbf{Dr}_\alpha] + c_\beta [Q(\mathbf{r}_\beta, t) + DQ_\beta \cdot \mathbf{Dr}_\beta]\} dS, \quad (18)$$

where the "vector"  $\mathbf{Dr}_\alpha$  has components  $(x-x_\alpha)^1 (y-y_\alpha)^m (z-z_\alpha)^n$ . Integrating  $\mathbf{Dr}_\alpha$  over the face gives the "vector" of geometric moments of the face,  $N_{\alpha\beta}(\mathbf{r}_\alpha)$ :

$$N_{\alpha\beta}^{lmn}(\mathbf{r}_\alpha) = \int_{\alpha\beta} \mathbf{Dr}_\alpha^{lmn} dS/S_{\alpha\beta} = \int_{\alpha\beta} (x-x_\alpha)^1 (y-y_\alpha)^m (z-z_\alpha)^n dS/S_{\alpha\beta} \quad (19)$$

The flux integral over face  $\alpha\beta$  now reduces to

$$\int_{\alpha\beta} \mathbf{n} \cdot \mathbf{F}^* dS = \mathbf{n}_{\alpha\beta} \cdot \frac{\partial F}{\partial Q} \{c_\alpha [Q(\mathbf{r}_\alpha, t) + DQ_\alpha \cdot N_{\alpha\beta}(\mathbf{r}_\alpha)] + c_\beta [Q(\mathbf{r}_\beta, t) + DQ_\beta \cdot N_{\alpha\beta}(\mathbf{r}_\beta)]\} S_{\alpha\beta}, \quad (20)$$

where the value of  $Q$  at the cell centroid can be obtained from the volume average as:

$$Q(\mathbf{r}_\alpha, t) = Q_\alpha(t) - DQ_\alpha \cdot M_\alpha(\mathbf{r}_\alpha). \quad (21)$$

The face integral can thus be expressed in terms of the known volume averages and the dot products  $DQ_\alpha \cdot [N_{\alpha\beta}(\mathbf{r}_\alpha) - M_\alpha(\mathbf{r}_\alpha)]$  and  $DQ_\beta \cdot [N_{\alpha\beta}(\mathbf{r}_\beta) - M_\beta(\mathbf{r}_\beta)]$ .

Substituting the representation for each DQ in terms of the neighbor moments and the volume averages (from the end of Section 3.4 above), one finally obtains after some collecting of terms:

$$\int_{\alpha\beta} \mathbf{n} \cdot \mathbf{F}^* dS = \mathbf{n}_{\alpha\beta} \cdot \frac{\partial F}{\partial Q} \sum_{\gamma} w_{\alpha\beta}^{\gamma} Q_{\gamma}, \quad (22)$$

where the weights  $w_{\alpha\beta}^{\gamma}$  are calculated from the various geometric moments of the neighbor cells and the face  $\alpha\beta$ .

## 4. Results and Discussion

### 4.1 Incident Field Computation

As discussed in the Introduction (Section 2), the first stage of simulation for the RAMS site is to determine the modifications to an incident plane wave caused by the interaction of the wave with the range profile, and specifically with the diffraction ridge leading down to the shadow pit. Because there is essentially no variation in the profile along the direction parallel to the ridge line, the only physically allowed variation of the fields in this direction is a phase factor  $\exp(ik_z z)$ , where  $k_z$  is the component of the incident wave vector  $\mathbf{k}$  parallel to the ridge line and  $z$  is distance along the ridge. The variation of the fields in the plane perpendicular to the ridgeline can thus be determined separately, as the solution to a two-dimensional boundary value problem.

To accurately simulate this problem within a finite computational domain, one must deal explicitly with the incident plane wave and its reflections off the flat sections of the range. These waves do not decay with distance from the ridge line, and thus will contribute substantially at the outer boundary of the domain. One can remove these contributions from the simulation by subtracting from the total field a solution of Maxwell's equations that incorporates this far-field behavior.

The Sommerfeld solution for scattering from a conducting half-plane provides the means to perform this subtraction, giving expressions for the fields in terms of easily evaluated Fresnel integrals. Considering the upper flat section from the illuminating radar to the ridge as an isolated half-plane, its solution  $E_u$  and  $H_u$  in the space above the ridge incorporates the behavior of the incident wave and its reflection from the upper half-plane (at the near-grazing incidence angles of interest for the range, the ground acts as an essentially perfect reflector). The reflection of the incident wave from the lower flat section beyond the ridge can be obtained from the reflection of the upper half-plane Sommerfeld solution about this lower plane, which will be denoted  $E_r$  and  $H_r$ .

The sum of these two special solutions satisfies the perfectly conducting boundary condition  $n \times E = 0$  on the lower flat section of the range, but  $n \times E_r$  does not vanish on the upper flat section. However, this upper section lies in the shadow of the reflected half-plane problem. As a consequence, when this sum is subtracted from the total field,  $E_r$  provides a source for the remainder, or diffracted, field on the upper half-plane that decays rapidly in strength with distance away from the ridge.

The other, and primary, source for the diffracted fields is the ridge profile that connects the two flat sections of the range. Here both  $E_u$  and  $E_r$  provide strong, non-vanishing tangential fields that will modify the plane-wave illumination of the target and its support. Gridding near this ridge must be dense enough to achieve accuracy in the phase and amplitude of the diffracted fields, and the grid between the ridge and the location of the target complex must be capable of propagating these fields accurately to the target site.

Outside of this critical region, only outgoing waves are present in the diffracted-field solution, and these decay in amplitude with distance from the ridge line. In the regions where this behavior obtains, grid density can be reduced rapidly without significantly affecting the

field values computed at the target site, and the computational domain can be terminated with a simple outgoing-wave condition on the fields.

A detail of the 2D grid near the ridge implementing these considerations is shown in Fig. 3. The grid resolution between the ridge and the target site was nowhere less than 20 points per wavelength at the simulation frequency of 131 MHz, which is near the lower limit of interest for RAMS; about 260,00 triangles composed this grid. Even at this low frequency, where diffraction effects are largest, one finds from the 2D simulation that the amplitude of the diffracted field at the target site is less than 3 % of the incident-wave amplitude.

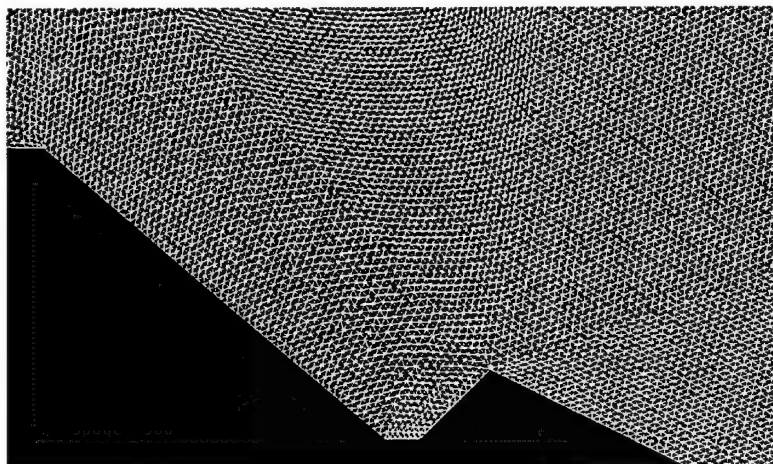


Fig. 3. Unstructured triangular grid in the vicinity of the diffraction ridge

The qualitative features of the diffracted-field solution are illustrated in Fig. 4. A cylindrical wave emanating from the ridge slope and a plane wave from the flat tail of the slope are the primary components. The strong cylindrical-wave diffraction off the top edge of the ridge has been subtracted out as part of the Sommerfeld solution. It is added back in for the second stage of the simulation, where the 3D scattering off the target and its support are computed. Its effects are evident in the total-field plot of Fig. 5, where the field is seen to be effectively nullified very close to the ridge and near the bottom of the shadow pit.



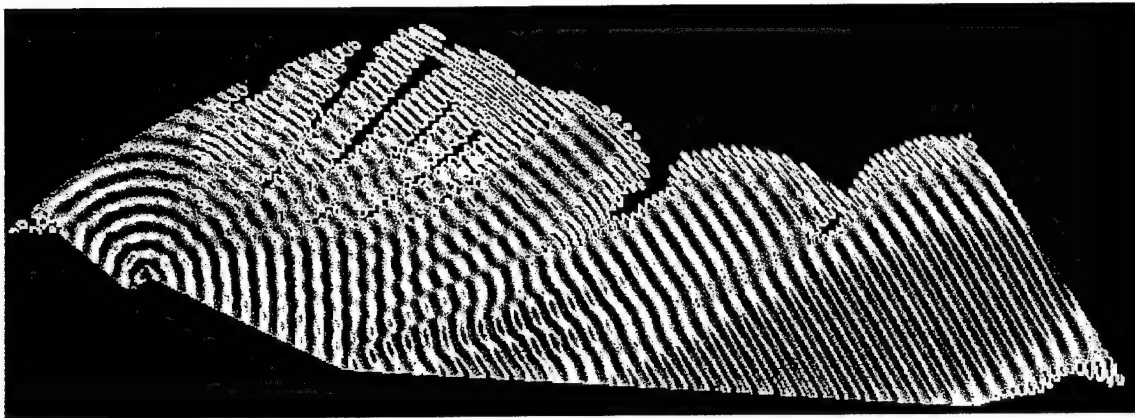


Fig. 4. Snapshot of the numerically generated diffracted electric field, which modifies the two half-plane solutions to produce the wave incident on the target and its support.

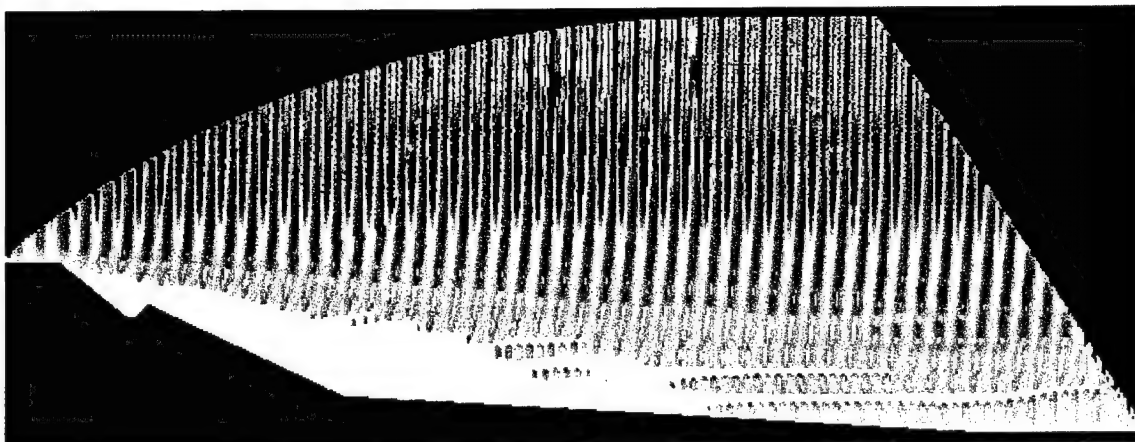


Fig. 5. Snapshot of the total electric field for the same conditions as in Fig. 4.

The final step of the 2D simulation is to store the amplitude and phase of the total tangential electric field at the centroid of each surface element on the target and its supporting pylon. These data provide the boundary values for the 3D simulation of scattering from the whole structure.

#### **4.2 3D Scattering Simulation: ORCA Target on the RAMS Pylon**

The purpose of these first 3D simulations is to determine the computational resources required to obtain results that will be useful for assessing range effects on the measured RCS

for Low Observable targets. Such a target has been designed and constructed at RATSCAT, a modified almond shape designated the ORCA (for Optimal Radiation Calibration Apparatus). It has a very low nose-on RCS over the band of frequencies between 120 and 600 MHz, and its return has been measured at RAMS over this band as a function of azimuth angle at zero elevation (a waterline cut). Figure 6 shows the ORCA geometry and a typical surface gridding for the target.

Various views of the unstructured 3D range grid generated for this simulation are shown in Fig. 6. This grid includes not only the range profile, but also the ORCA and the RAMS pylon. It was generated automatically from 2D triangular grids on each section of surface enclosing the computational domain, including the outer boundary. A moderate resolution of 20 points per wavelength was maintained at the target edges, and the minimum resolution between the target and the diffraction ridge was 10 points per wavelength. To simplify the grid generation for these tests, the vertical plane bisecting the pylon was taken as a symmetry plane, with the ridge line reoriented perpendicular to this plane. The resulting grid contained 630,000 tetrahedral cells in the half-space to one side of the symmetry plane.

The 3D scattered-field simulations could be run efficiently on as few as 8 nodes of an IBM SP2, and test runs were made on 8, 16, 32, and 64 nodes to verify that nearly linear speedup could be obtained. A typical run on 64 nodes took less than an hour using the current version of the unstructured-grid solver UPRCS. This version has not been optimized for the application of modified incident fields at the conducting boundaries, and does not yet incorporate the high-order corrections outlined in Section 3. It employs fourth-order Runge-Kutta time integration.

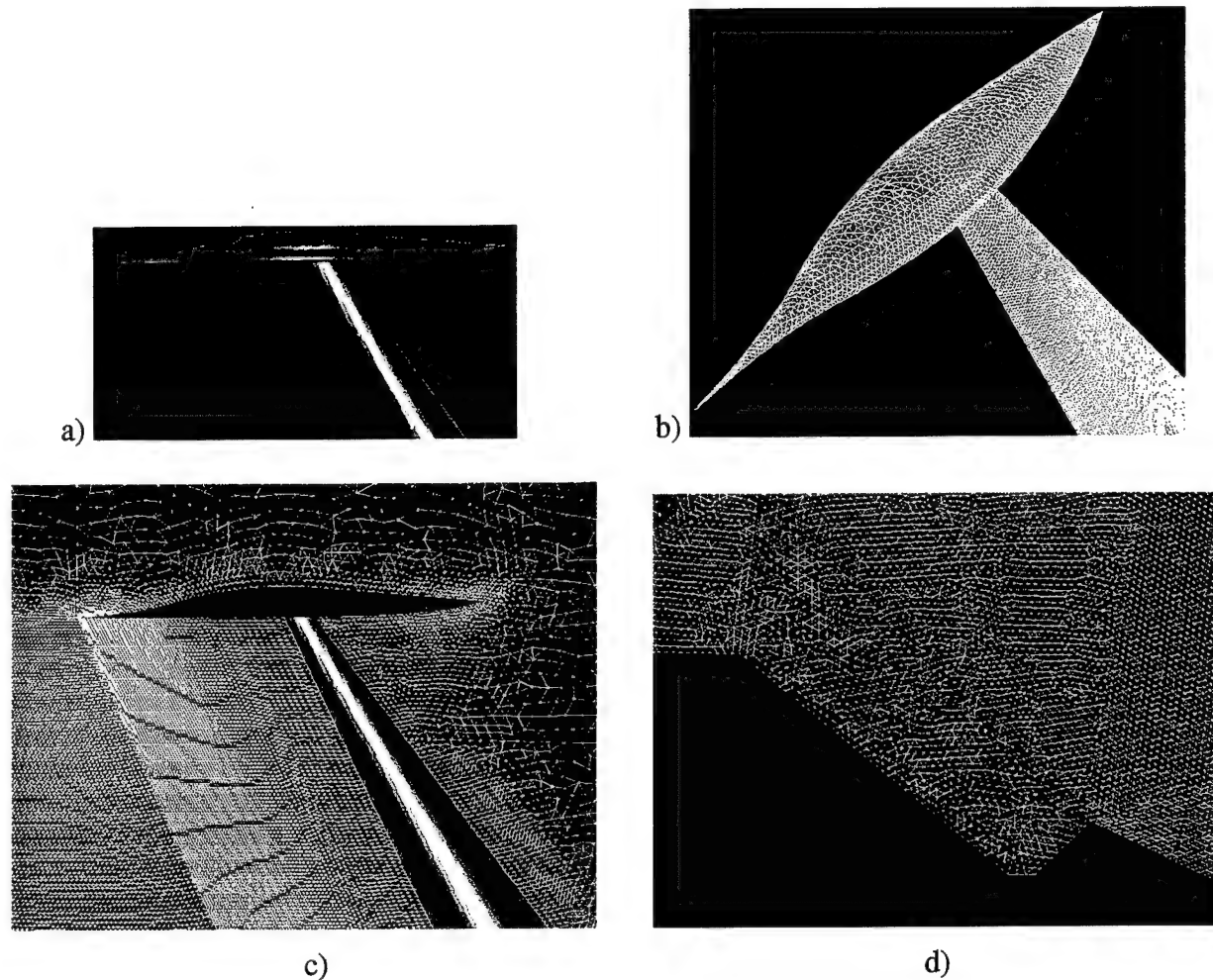


Fig. 6. ORCA and pylon 3D gridding: a) ORCA/pylon geometry; b) Surface grid on ORCA and pylon; c) The triangular grid on the symmetry plane behind the pylon; d) Symmetry plane grid near the ridge

Results for the scattered and total electric field parallel to the ridge line are shown in Figs. 7 and 8 for the case of a horizontally-polarized 131 MHz incident wave. The ORCA is oriented nose-on to the illuminating radar, and the angle of incidence is chosen to place the ORCA at the first maximum in the electric field created by the incident plane wave and its reflection in the upper half-plane. To derive the radar return from these simulations, one must integrate the surface currents induced on the target, pylon, and ground with the appropriate far-field Green's function (which includes diffraction off the edge of the upper half-plane). However, one can already observe in these figures a definite effect of the pylon on the

scattering, which will show up in the measured RCS. A simulation without the pylon, including only the ORCA suspended above the shadow pit, would provide a direct measure of the impact of the pylon on the RCS.

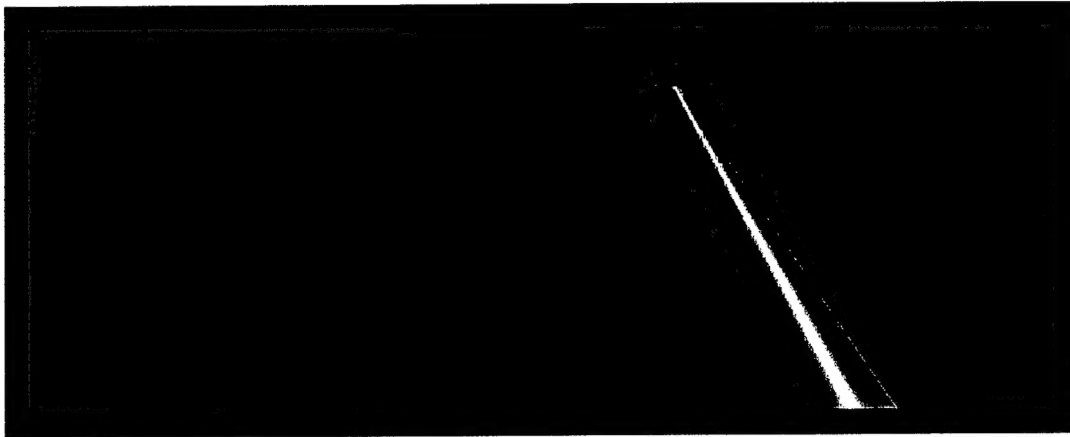


Fig. 7. Scattered E field (component parallel to ridge line) within the shadow pit at 131 MHz for H-polarized incident wave

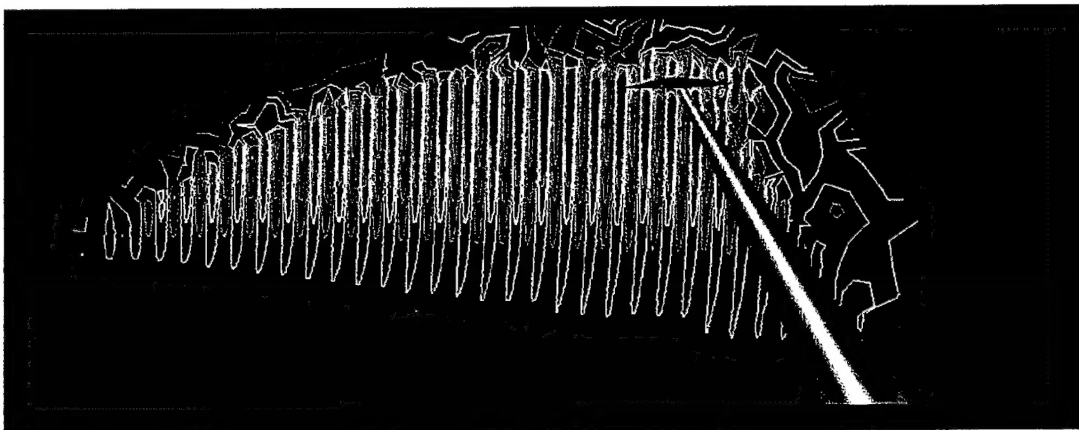


Fig. 8. Total E field (component parallel to ridge line) within the shadow pit at 131 MHz for H-polarized incident wave

#### 4.3 Grid Sensitivity Test: The Business Card

A major reduction in sensitivity of the solution to details of gridding has been demonstrated with the new code UPRCS, which implements an unstructured-grid fourth-order Runge-Kutta integration scheme of the type outlined in Section 3.2.3.3. In Fig. 9 results for the RCS of a thin rectangular plate illuminated near grazing incidence are plotted for two radically

different grids: an unstructured triangular grid extruded into prisms normal to the plate, and a structured rectangular grid, extruded in the same way. Both grids have been clustered near the edges of the plate to better model the singular behavior of the fields at these edges. The dimensions of this plate are those of the Electromagnetic Code Consortium Test Case 4, and the conditions match those of the range measurements made at NAWC-China Lake.

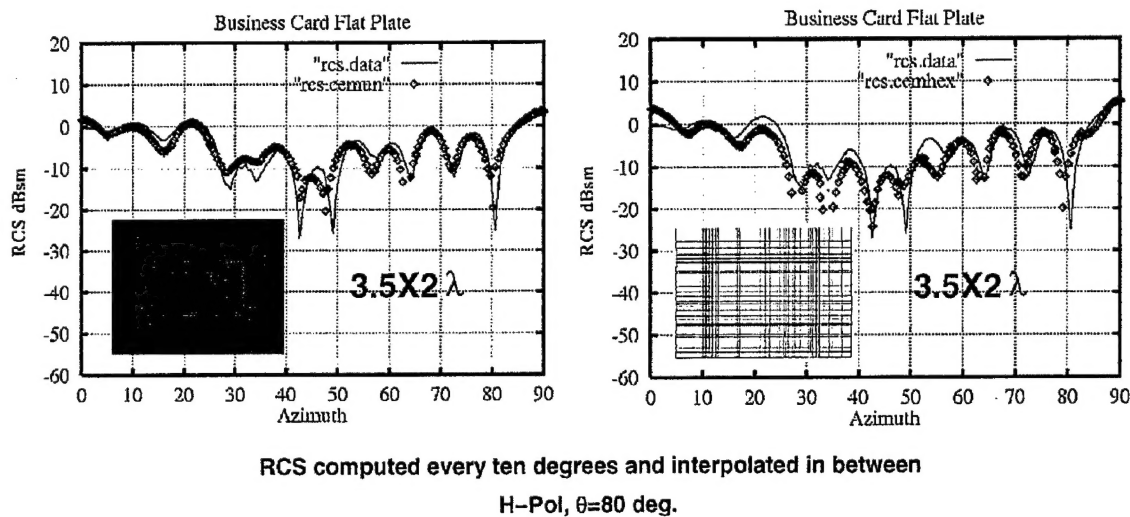


Fig. 9. Grid Insensitivity of UPRCS: Comparison of business card RCS results for an unstructured and a structured grid with range measurements

Test Case 4 proved to be difficult for many of the codes tested by the Consortium, largely because of the dominant traveling-wave contribution to the RCS near zero azimuth. To obtain satisfactory accuracy with the original Rockwell upwind code RCS3D, the clustering of structured cells at the plate edges had to approach 50 points per wavelength. In contrast, UPRCS achieves the same level of agreement with no more than 30 points per wavelength. Of more significance for this study, essentially the same results are obtained for the unstructured triangular cross-section grid at the same level of resolution. The first Rockwell unstructured-grid solver RCSUN (also employing a pure upwind algorithm) required about three times as many cells to obtain a satisfactory result.

The algorithm in UPRCS has removed two sources of error present in the earlier codes: excessive damping and inaccurate extrapolation to the cell faces. It is anticipated that implementing the high-order extrapolations outlined in Section 3 will further improve the accuracy of the method at moderate resolution, and will also increase the robustness of the results in the presence of irregular grid cells, which are a common feature of automatically-generated grids.

## **5. Conclusions**

The initial radar range simulation results presented here demonstrate that the methods for time-domain integration of Maxwell's equations have reached a stage where present-day high performance computers can be used to explore and improve upon range design, based on direct computation of the radar return at frequencies below 600 MHz. Opportunities for increasing the accuracy and efficiency of the integration methods on unstructured grids have also been identified, and these possibilities are being actively pursued. In the long term, improvements to the basic algorithms will allow these methods to be applied to more difficult optimization scenarios and higher frequencies. In the near term, one can undertake detailed studies of many experimental schemes for extending accurate RCS measurements to lower frequency on existing radar ranges.

## 6. References

1. Rowell, C., Shankar, V., Hall, W. F., and Mohammadian, A., "Algorithmic aspects and computing trends in computational electromagnetics using massively parallel architectures," presented at the First IEEE Conference on Algorithms and Architectures for Parallel Processing, Brisbane, April, 1995
2. Mohammadian, A. H., Shankar, V., and Hall, W. F., "Computation of electromagnetic scattering and radiation using a time-domain finite-volume discretization procedure," *Computer Phys. Comm.* **68**, 175 (1991)
3. Yee, K. S., "Numerical solution of initial boundary value problems involving Maxwell's equations in isotropic media," , *IEEE Trans. Antennas Propagat.* **14**, 302 (1966)
4. Gedney, S. and Lansing, F., "A parallel discrete surface integral equation method for the analysis of three-dimensional microwave circuit devices with planar symmetry," *IEEE Antennas Propagat. Symp. Dig.* **3**, 1778, Seattle, 1994
5. Madsen, N. K., "Divergence preserving discrete surface integral methods for Maxwell's curl equations using non-orthogonal unstructured grids," *J. Comput. Phys.* **119**, 34 (1995)
6. Yee, K. S., and Chen, J. S., "The FDTD and FVTD Methods in Solving Maxwell's Equations," *IEEE Trans. Antennas Propagat.* **45**, 354 (1997)
7. Barth, T.J., "Recent developments in high order k-exact reconstruction on unstructured meshes," AIAA Paper 93-0668, January, 1993
8. Frink, N.T., "Recent progress toward a three-dimensional unstructured Navier-Stokes flow solver," AIAA Paper 94-0061, January, 1994
9. Jameson, A., "Successes and challenges in computational aerodynamics," AIAA paper 87-1184, Proceedings of the 8<sup>th</sup> AIAA Computational Fluid Dynamics Conference, 1987
10. Thomas, J. P., and Roe, P. L., "Development of non-dissipative numerical schemes for computational aeroacoustics," AIAA paper 93-3382, 1993
11. Palaniswamy, S., Hall, W. F., and Shankar, V., "Numerical solution to Maxwell's equations in the time domain on nonuniform grids," *Radio Science*, July/August, 1996